NANO LETTERS

2003
Vol. 3, No. 10
1425−1429

Continuous Hot Wire Chemical Vapor Deposition of High-Density Carbon Multiwall Nanotubes

Anne C. Dillon,* A. Harv Mahan, Philip A. Parilla, Jeffery L. Alleman, Michael J. Heben, Kim M. Jones, and Katherine E. H. Gilbert

National Renewable Energy Laboratory, 1617 Cole Blvd, Golden, Colorado 80401

Received April 4, 2003; Revised Manuscript Received June 13, 2003

ABSTRACT

Hot wire chemical vapor deposition (HWCVD) has been adapted to be a continuous growth process for high-density carbon multiwall nanotubes (MWNTs). MWNT growth is optimized in 1:5 CH_4:Ar at 150 Torr with reactor temperatures of 400 and 550 °C for static and flowing gases, respectively. Ferrocene is employed to provide a gas-phase catalyst. Highly graphitic nanotubes can be continuously deposited with iron content as low as 15 wt % and carbon impurities below thermal gravimetric analysis detection limits. The MWNTs are simply purified to ∼99.5 wt % with minimal structural damage and with a 75 wt % yield.

Carbon multiwall nanotubes (MWNTs) are promising for multiple applications including strong composite materials, field emission displays, and adsorbents for gas separation or storage. A continuous low-cost production method for easily purified MWNTs is therefore desired. MWNTs were discovered while vaporizing carbon in an electric arc[1] and were then produced at higher yield by increasing the pressure of the helium gas atmosphere.[2] Chemical vapor deposition (CVD) techniques employing benzene pyrolosis,[3] and the decomposition of ethylene[4] and acetylene[5] on supported metal catalysts were also demonstrated as viable large-scale production methods. Recently, MWNTs have been grown on supported metal particles or films via CVD,[6−10] plasma enhanced CVD,[11−21] hot wire chemical vapor deposition (HWCVD),[22,23] and plasma enhanced HWCVD methods.[24,25] Also, one HWCVD report employed evaporation of the Fe−Cr filament to supply a gas-phase catalyst, resulting in MWNTs with a high density of structural defects and significant carbon impurities.[26] Although more research is necessary, this particular HWCVD method has potential for large-scale production since it is not substrate dependent.

In 1997[27] and 1998,[28] ferrocene provided a gas-phase catalyst for continuous MWNT formation from methane at 1150 °C. However, the 1997 study reported materials containing more amorphous carbon than arc-generated MWNTs, presumably due to a lower synthesis temperature than that achieved in the arc process.[27] In the 1998 study, the outer layers of the tubes were not graphitic.[28] Later, ferrocene and ethylene were employed in CVD of MWNTs between 650 and 950 °C.[29] Again carbon impurities were observed at high density. The authors concluded that further work was necessary to improve the nanotube microstructure and yield.[29] High-purity aligned, graphitic MWNTs were synthesized via decomposition of a ferrocene−xylene mixture at ∼675 °C. However, although the catalyst was supplied in the gas phase, nucleation of tube growth occurred only for iron species deposited on a quartz substrate, resulting in a surface growth mechanism and limiting yields to available surface area.[30]

Here, the first continuous high-density MWNT gas-borne formation is demonstrated with HWCVD, and all of the MWNTs are highly graphitic. A wide diameter distribution of nanotubes is obtained for the optimal conditions of this process with the MWNTs containing approximately 2−20 concentric shells with inner and outer tube diameters of approximately 3−15 and 5−25 nm, respectively. The as-produced materials have low metal contents of 15−25 wt % and nonnanotube carbon contents ranging from ∼10 wt % down to levels that are undetectable with thermal gravimetric analysis (TGA). Furthermore, the MWNTs are easily purified to >99 wt % without detectable structural damage and with 60−75 wt % yields. To date, the best quantitative purification technique resulted in MWNT nanotube purity of >94% and ∼50% yield.[31] However, these purified nanotubes were oxidized at a lower temperature than the raw nanotubes, indicating that defects or reactive functional groups were introduced during purification.[31] Another nondestructive purification method resulted in 91% pure tubes and a yield of 17%.[32]

In this study, the depositions are performed in a quartz tube reactor enclosed in a clamshell furnace. Two physically

* Corresponding author. E-mail: adillon@nrel.gov.

10.1021/nl0342038 CCC: $25.00
Published on Web 09/06/2003

parallel 0.5 mm tungsten filaments ~15 cm in length are operated in series at ~20 A, 25 V, and at 2000 °C as determined by an optical pyrometer. Ferrocene is used to supply an iron catalyst by maintaining the powder source near the sublimation temperature (140 °C), and methane is the primary carbon source. The furnace temperature is varied between room temperature and 1200 °C, and various methane concentrations in argon are explored. Under optimal conditions, graphitic MWNTs with minimal carbon impurities are produced in 1:5 CH_4/Ar at 150 Torr at ~100 mg/hr with the furnace at 400 °C in a static gas environment or at ~150 mg/hr with gas flow rates of 20 (CH_4) and 100 (Ar) sccm and the furnace at 550 °C. The raw materials are purified with a 16 h reflux in 3M nitric acid at 120 °C. The MWNTs are recovered via filtration on a hydrophilic polypropylene filter, rinsed with deionized water and dried at 60 °C for ~1 h. To remove intercalated nitric acid, the purified materials are degassed in a vacuum to 550 °C. TGA in a TA SDT2960 with a heating rate of 20 °C/min in flowing "dry air" (80% N_2, 20% O_2) at 100 sccm is used to determine MWNT purity.

Figure 1a displays a transmission electron microscope (TEM) image of MWNTs produced in static 1:5 CH_4/Ar at 400 °C. Iron particles approximately 10−25 nm in diameter are also apparent, but carbon impurities are not readily detected in this or other images of the crude soot. Similar material is observed at ~50% higher growth rate with flowing gases at 550 °C. The increase in furnace temperature most likely compensates for the continuous flowing of room-temperature gases. Figure 1b displays high-resolution TEM images showing the MWNTs are graphitic with the distance between layers measuring ~0.34 nm.

Surprisingly, these crystalline tubes are produced at a lower furnace temperature than that employed in most MWNT CVD processes (~650−1150 °C). During deposition, a black carbon soot is deposited throughout the reactor, coating the quartz walls, electrical feed-throughs, and ceramic insulators. The thickness of the carpet-like deposit increases with reaction duration and the density of MWNTs in the deposit scales with the filament length. In the flowing environment, carbon soot migrates downstream and deposits outside the hot zone. MWNT formation is not observed without operating the filaments for furnace temperatures as high as 800 °C; however, some carbon deposition occurs due to thermal dissociation of the ferrocene and/or methane. Together these data indicate that the MWNT growth is initiated at elevated temperature *near* the filaments,[33] allowing for a decreased external furnace temperature. The data are also consistent with a gas-borne growth mechanism. The MWNT growth is most likely quenched upon migration to cooler temperature zones.

Figure 2a displays the TGA curves of crude MWNT soot produced at optimal conditions and the same material following purification. The crude material weight shows a slight initial increase consistent with the oxidation of iron catalyst particles between 250 and 450 °C. The simultaneous temperature difference signal for the crude material (not shown) indicates combustion of a single carbon phase

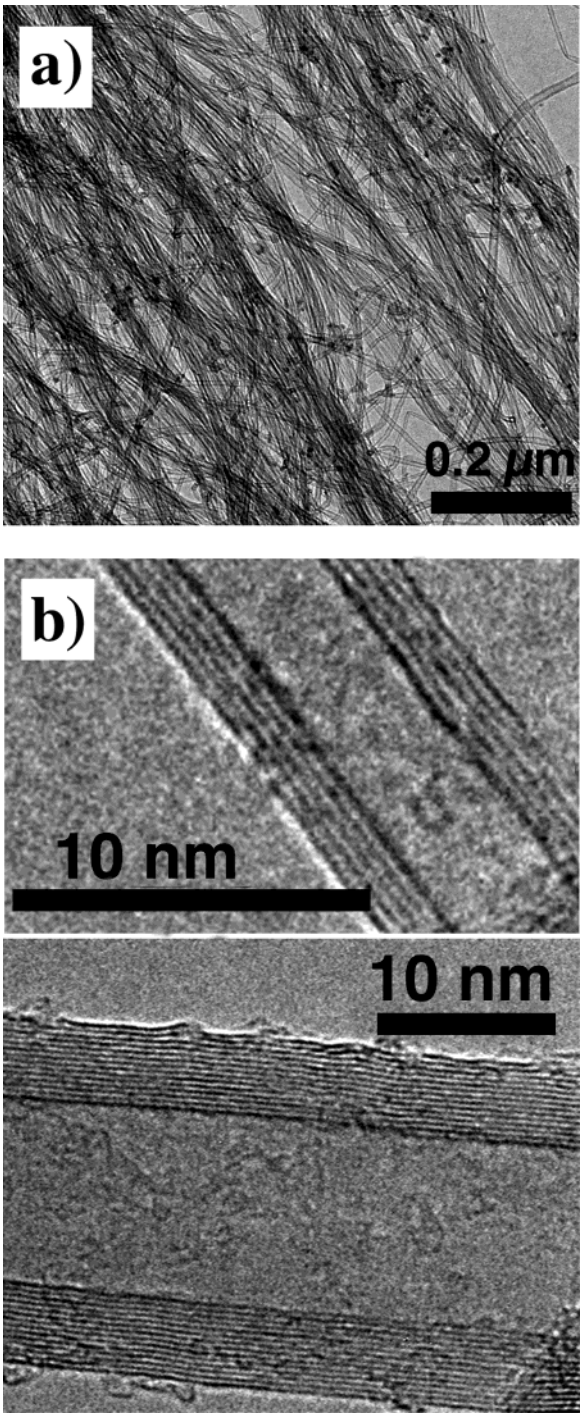

Figure 1. TEM images of (a) MWNTs produced with optimized HWCVD conditions, 1:5 CH_4/Ar and 400 °C furnace and (b) the graphitic nature of these tubes revealed at higher magnification.

(MWNTs) maximized at 592 °C. A material fraction of ~20 wt % remains and corresponds to Fe oxide residue. (No tungsten is detected with energy dispersive spectrometry, indicating that for these operating conditions the filament does not decompose.) The remaining weight fraction in Figure 2a is then consistent with ~15 wt % iron in the crude soot. The TGA curve of the purified material (Figure 2a) shows that decomposition again occurs in a single phase with the simultaneous temperature difference maximized at 680 °C. The lower decomposition temperature for the MWNTs

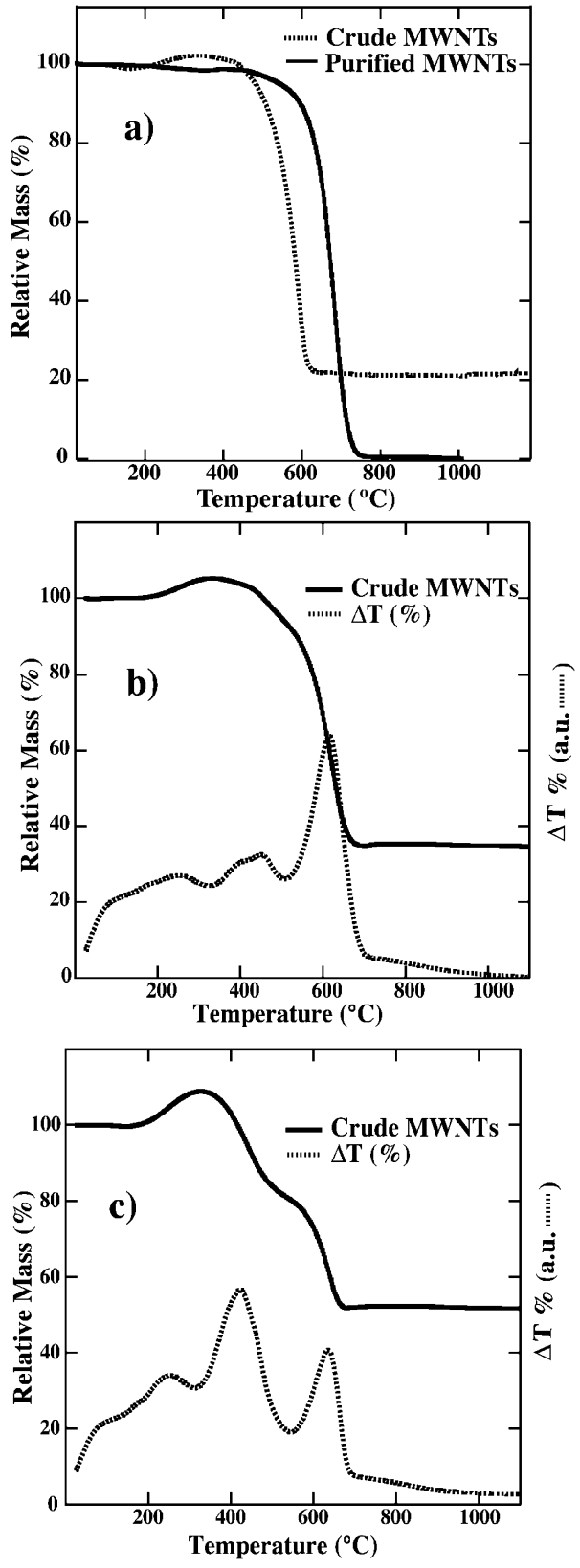

Figure 2. TGA curves showing (a) the oxidation of HWCVD crude MWNT soot produced at optimal conditions and the same material following purification with a dilute nitric acid reflux, (b) the oxidation of HWCVD crude MWNT soot produced at optimal conditions but containing ~10 wt % nonnanotube carbon impurities, and (c) the oxidation of HWCVD crude MWNT soot produced at nonoptimal conditions (CH_4/Ar, 1:1). The simultaneous temperature difference curves are also shown in (b) and (c).

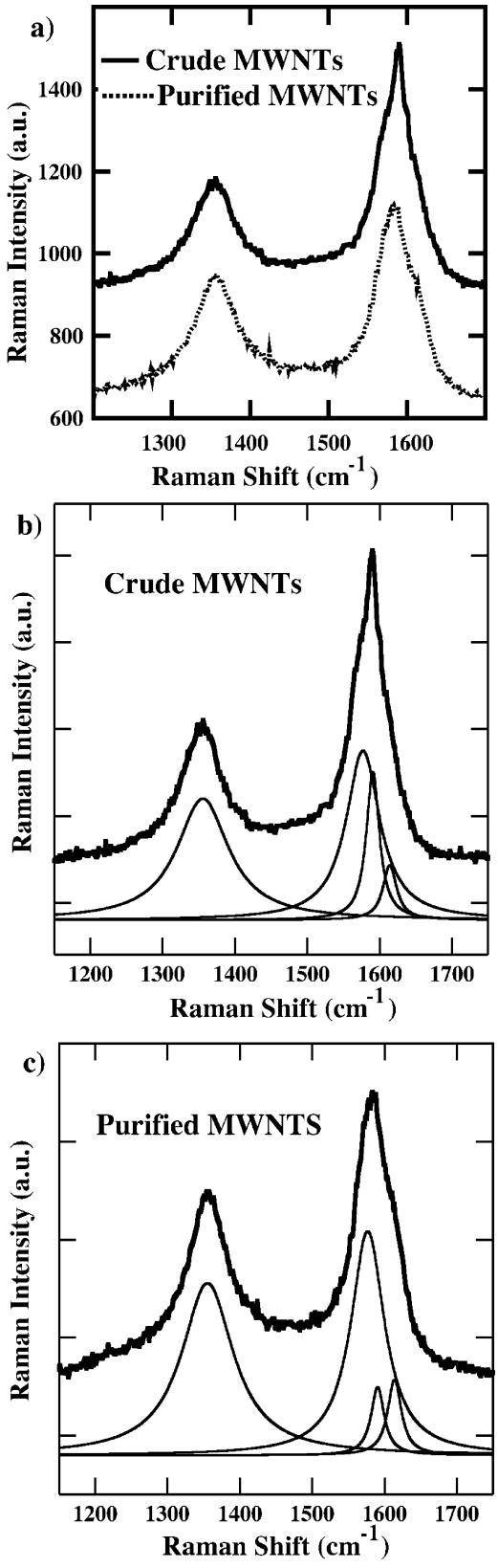

Figure 3. Raman spectra of (a) the HWCVD crude MWNT soot produced at optimal conditions and the same material following purification, (b) the spectrum of the crude material and the four Lorentzian peak fits, and (c) the spectrum of the purified material and the four Lorentzian peak fits. Raman spectroscopy is performed with a resolution of 2−4 cm^{-1} using ~7 mW of the 488 nm line of an Ar ion laser. There is an offset in (a) to aid the visualization of the spectra.

Table 1. Fits to the Raman Spectra for the Crude and Purified MWNTs Including Four Lorentzians for Each Spectrum[a]

peak location (cm^{-1})	peak fwhm (cm^{-1})	crude peak area (% total)	purified peak area (% total)	pure/crude ratio	ratio normalized to D-band
1355.33	87.19	42.86	48.48	1.131	1.000
1576.95	56.82	38.95	41.13	1.056	0.934
1590.65	21.91	13.13	4.81	0.367	0.324
1614.05	22.91	5.07	5.58	1.101	0.974

[a] The peak locations and fwhms are common between the two spectra and the amplitudes are independent. The data show that the peak at 1591 cm^{-1} decreases drastically for the purified sample compared to the crude sample.

in the crude soot is consistent with exothermic combustion of the metal particles, resulting in localized hot spots that initiate early tube oxidation. After the complete combustion of the purified MWNTs, a small remaining particle was removed and weighed with a microbalance to eliminate TGA drift. The particle weighed 25 μg $\pm$10%, indicating the nanotubes are ~99.5 wt % pure.

Figure 2b displays the TGA curve of a crude MWNT soot also produced under optimal conditions. However, in this case ~10 wt % carbon impurities are detected by TGA, as weight loss now occurs as early as ~375 °C. Transmission electron microscopy confirmed the presence of nanoparticle carbon. The simultaneous temperature difference signal for this TGA curve is also shown in Figure 2b and indicates that combustion of the nonnanotube carbon phase is maximized at 453 °C and the combustion of the MWNTs is maximized at 615 °C. For this sample, the ~10 wt % carbon impurities as well as the ~26 wt % metal were digested in the dilute nitric acid reflux, and a sample that was >99 wt % pure MWNTs was obtained.

Figure 2c displays a TGA curve of a crude MWNT sample that was produced under nonoptimal conditions with a CH_4/Ar ratio of 1:1 instead of 1:5 (optimal). For this sample, TEM revealed that the nanotubes were highly coated with nanoparticle carbon. The simultaneous temperature difference signal for this TGA curve (Figure 2c) is again shown and indicates that the combustion of the nonnanotube carbon phase is maximized at 420 °C and the combustion of the MWNTs is maximized at 633 °C. The TGA curve suggests that the sample has >20 wt % nonnanotube carbon as well as ~39 wt % metal. It is unlikely that nonnanotube carbon at this higher level would be completely digested with the dilute nitric acid reflux employed in this purification process. However, the carbon impurities may be removed by air oxidation at ~420 °C prior to the acid reflux, as indicated by the simultaneous temperature difference signal of Figure 2c, or by air oxidation at approximately the same temperature following the acid reflux as previously demonstrated for carbon single-wall nanotubes.[34]

Raman spectroscopy was employed to further evaluate the MWNTs. Figure 3a displays Raman spectra for MWNTs produced with optimal synthesis conditions before and after purification. In both spectra, features at ~1590 and 1355 cm^{-1} are consistent, respectively, with the in-plane carbon stretching mode (G-band) and a disorder-induced vibrational mode (D-band) associated with either MWNT finite size effects and structural defects[35] or the presence of nanocrystalline graphite impurities.[36,37] The D-band/G-band intensity (D/G) ratio in the spectrum of the as-produced HWCVD nanotubes is ~0.40, indicating that these MWNTs are more completely graphitized and/or contain fewer carbon impurities than other CVD-generated MWNTs where the D/G ratio is $\geq$1.[8,12,13,18,19,26] However, a similar[14,16,17,20] and slightly smaller[38] D/G ratio than that observed here has also been previously reported for unpurified CVD-generated MWNTs.

The G-bands of the MWNT materials in Figure 3a are highly asymmetric, indicating that they are a superposition of more than one peak. A shoulder at ~1614 cm^{-1} appears in both spectra consistent with previous Raman characterization of MWNTs.[38] Upon purification, a decrease in the sharp feature centered at 1591 cm^{-1} is strikingly apparent. The change in shape of the purified material G-band is perhaps consistent with the digestion of smaller diameter or more defective, less stable MWNTs during the HNO_3 reflux. To further quantify the decrease in the sharp feature at 1591 cm^{-1}, the original Raman spectra of both the crude and purified materials were fit to a model. The model consists of four Lorentzians (one for the D-band and three for the tangential modes[38]) superimposed with a cubic background. Both curves were fit simultaneously with the constraints that the corresponding peaks in the two traces could have different amplitudes but their positions and full-widths-at-half-maximums (fwhms) were common. Similarly, the linear, quadratic and cubic terms of the background were common for the two traces and the constant term could be different.

Figures 3b and 3c show the initial spectra and the resulting Lorentzian fits for the crude and purified materials, respectively. It should be noted that absolute peak amplitudes between the two traces cannot be directly compared due to nonequivalent optical collection efficiencies for the two samples. Quantitative comparisons must be based on the relative changes of the component peaks. Table 1 contains the numerical results and shows that the area of the peak at 1591 cm^{-1} is reduced to about 1/3 of its original value after purification while the other peaks remain roughly constant in magnitude. This is further borne out if the data is normalized to the D-band peak so that a more direct comparison of the two traces is possible. Although a direct absolute comparison is not possible, it is interesting to note that the Raman fits predict an ~15 wt % nanotube loss. A 75 wt % yield was recovered for this sample following purification, indicating that the 15 wt % metal and ~10 wt % carbon nanotubes were consumed. The experimental results are thus in reasonably good agreement with the data predicted from the curve fitting analysis.

Modification of the synthesis parameters from optimal conditions causes MWNT contents in the carbon soots to decline. For example, when the external furnace temperature is decreased below 400 °C, the amount of nanocrystalline graphite and/or amorphous carbon increases. Graphitic MWNTs are not formed in room-temperature depositions. When the furnace temperature is elevated above 650 °C, larger nonnanotube graphitic structures are frequently observed. Above 1000 °C micron-sized graphitic particles, sheets, and onions are formed and MWNTs are no longer detected with TEM. The MWNT growth is optimized with the external furnace between 400 and 550 °C. The mechanistic aspects leading to this optimization are not yet clear, but the relative stability of nuclei in the near-filament region is probably important. Additionally when the carbon precursor concentration is increased to 1:1 CH_4/Ar or decreased to 1:20 CH_4/Ar, more amorphous carbon and nanocrystalline graphite is observed. Optimal nanotube growth for a carbon precursor concentration of 1:5 CH_4/Ar may be explained with nucleation and kinetic considerations. MWNTs are nucleated on the metal particles and growth in length occurs as carbon atoms are added. If the carbon mass transfer is too low, nanotube nucleation may not occur. For higher carbon mass transfer, however, more gas borne carbon nanoparticles are formed. The metal particles may then be coated with these carbon impurities, terminating MWNT production.

This HWCVD method represents the first continuous gas-borne production of graphitic MWNTs at high density that are simply purified to 99.5 wt %. Since both the synthesis and purification techniques described here may be easily and economically scaled, this work could facilitate industrial production of carbon MWNTs.

Acknowledgment. This work was supported by the DDRD program at NREL and by the Office of Science, Basic Energy Sciences, Division of Materials Science under subcontract DE-AC02-83CH10093.

References

(1) Iijima, S. *Nature* **1991**, *354*, 56.
(2) Ebbesen, T. W.; Ajayan, P. M. *Nature* **1992**, *358*, 220.
(3) Endo, M.; Takeuchi, K.; Igarashi, S.; Kobori, K.; Shiraishi, M.; Kroto, H. W. *J. Phys. Chem. Sol.* **1993**, *54*, 1841.
(4) Jose-Yacaman, M.; Miki-Yoshida, M.; Rendon, L.; Santiesteban, J. G. *Appl. Phys. Lett.* **1993**, *62*, 202.
(5) Ivanov, V.; Nagy, J. B.; Lambin, P.; Lucas, A.; Zhang, X. B.; Zhang, X. F.; Bernaerts, D.; Van Tendeloo, G.; Amelinckx, S.; Van Landuyt, J. *Chem. Phys. Lett.* **1994**, *223*, 329.
(6) Thong, J. T. L.; Oon, C. H.; Eng, W. K.; Zhang, W. D.; Gan, L. M. *Appl. Phys. Lett.* **2001**, *79*, 2811.
(7) Tang, D. S.; Xie, S. S.; Pan, Z. W.; Sun, L. F.; Liu, Z. Q.; Zou, X. P.; Li, Y. B.; Ci, L. J.; Liu, W.; Zou, B. S.; Zhou, W. Y. *Chem. Phys. Lett.* **2002**, *356*, 563.
(8) Lee, C. J.; Kim, D. W.; Lee, T. J.; Choi, Y. C.; Park, Y. S.; Kim, W. S.; Lee, Y. H.; Choi, W. B.; Lee, N. S.; Kim, J. M.; Choi, Y. G.; Yu, S. C. *Appl. Phys. Lett.* **1999**, *75*, 1721.
(9) Xie, S.; Li, W.; Pan, Z.; Chang, B.; Sun, L. *Mater. Sci. Engin. A* **2000**, *286*, 11.
(10) Li, Y. J.; Sun, Z.; Lau, S. P.; Chen, G. Y.; Tay, B. K. *Appl. Phys. Lett.* **2001**, *79*, 1670.
(11) Qin, L. C.; Zhou, D.; Krauss, A. R.; Gruen, D. M. *Appl. Phys. Lett.* **1998**, *72*, 3437.
(12) Chen, M.; Chen, C.-M.; Chen, C.-F. *J. Mater. Sci.* **2002**, *37*, 3561.
(13) Choi, Y. C.; Bae, D. J.; Lee, Y. H.; Lee, B. S.; Park, G.-S.; Choi, W. B.; Lee, N. S.; Kim, J. M. *J. Vac. Sci. Technol. A* **2000**, *18*, 1864.
(14) Chung, S. J.; Lim, S. H.; Lee, C. H.; Jang, J. *Diamond Relat. Mater.* **2001**, *10*, 248.
(15) Ho, G. W.; Wee, A. T. S.; Lin, J.; Tiju, W. C. *Thin Solid Films* **2001**, *388*, 73.
(16) Wang, H.; Lin, J.; Huan, C. H. A.; Dong, P.; He, J.; Tang, S. H.; Eng, W. K.; Thong, T. L. J. *Appl. Surf. Sci.* **2001**, *181*, 248.
(17) Zhang, Q.; Yoon, S. F.; Ahn, J.; Gan, B.; Rusli; Yu, M.-B. *J. Mater. Res.* **2000**, *15*, 1749.
(18) Yoon, H. J.; Kang, H. S.; Shin, J. S.; Son, K. J.; Lee, C. H.; Kim, C. O.; Hong, J. P.; Cha, S. N.; Song, B. G.; Kim, J. M.; Lee, N. S. *Physica B* **2002**, *323*, 344.
(19) Woo, Y. S.; Jeon, D. Y.; Han, I. T.; Lee, N. S.; Jung, J. E.; Kim, J. M. *Diamond Relat. Mater.* **2002**, *11*, 59.
(20) Lee, H.; Kang, Y.-S.; Lee, P. S.; Lee, J.-Y. *J. Alloys Compd.* **2002**, *330*, 569.
(21) Bower, C.; Zhou, O.; Zhu, W.; Werder, D. J.; Jin, S. *Appl. Phys. Lett.* **2000**, *77*, 2767.
(22) Park, K. H.; Lee, K. M.; Choi, S.; Lee, S.; Koh, K. H. *J. Vac. Sci. Technol. B* **2001**, *19*, 946.
(23) Ono, T.; Miyashita, H.; Esashi, M. *Nanotechnology* **2002**, *13*, 62.
(24) Han, J.-h.; Moon, B.-S.; Yang, W. S.; Yoo, J.-B.; Park, C. Y. *Surf. Coat. Technol.* **2000**, *131*, 93.
(25) Ren, Z. F.; Huang, Z. P.; Xu, J. W.; Wang, J. H.; Bush, P.; Siegal, M. P.; Provincio, P. N. *Science* **1998**, *282*, 1105.
(26) Chen, C.-F.; Lin, C.-L.; Wang, C.-M. *Jpn. J. Appl. Phys.* **2002**, *41*, L67.
(27) Qin, L. C. *J. Mater. Sci. Lett.* **1997**, *16*, 457.
(28) Fan, Y.-Y.; Li, F.; Cheng, H.-M.; Su, G.; Yu, Y.-D.; Shen, Z.-H. *J. Mater. Res.* **1998**, *13*, 2342.
(29) Marangoni, R.; Serp, P.; Feurer, R.; Kihn, Y.; Kalck, P.; Vahlas, C. *Carbon* **2001**, *39*, 443.
(30) Andrews, R.; Jacques, D.; Rao, A. M.; Derbyshire, F.; Qian, D.; Fan, X.; Dickey, E. C.; Chen, J. *Chem. Phys. Lett.* **1999**, *303*, 467.
(31) Hou, P. X.; Bai, S.; Yang, Q. H.; Liu, C.; Cheng, H. M. *Carbon* **2002**, *40*, 81.
(32) Murphy, R.; Coleman, J. N.; Cadek, M.; McCarthy, B.; Bent, M.; Drury, A.; Barklie, R. C.; Blau, W. J. *J. Phys. Chem B* **2002**, *106*, 3087.
(33) Goodwin, D. G. *MRS Symp. Proc.* **1999**, *557*, 79.
(34) Dillon, A. C.; Gennett, T.; Jones, K. M.; Alleman, J. L.; Parilla, P. A.; Heben, M. J. *Adv. Mater.* **1999**, *11*, 1354.
(35) Bacsa, W. S.; Ugarte, D.; Chatelain, A.; de Heer, W. A. *Phys. Rev. B* **1994**, *50*, 15473.
(36) Eklund, P. C.; Holden, J. M.; Jishi, R. A. *Carbon* **1995**, *33*, 959.
(37) Wang, Y.; Alsmeyer, D. C.; McCreedy, R. L. *Chem. Mater.* **1990**, *2*, 557.
(38) Rao, A. M.; Jorio, A.; Pimenta, M. A.; Dantas, M. S. S.; Saito, R.; Dresselhaus, G.; Dresselhaus, M. S. *Phys. Rev. Lett.* **2000**, *84*, 1820.

NL0342038